Microbeam X-ray analysis of Ce^{3+}/Ce^{4+} in Ti-rich minerals: A case study with titanite (sphene) with implications for multivalent trace element substitution in minerals

Penelope L. King[1,2,3], Tsun-Kong Sham[4], Robert A. Gordon[5] & M. Darby Dyar[6]

1. Department of Earth Sciences, The University of Western Ontario, London ON N6A 5B7 Canada.
2. Institute of Meteoritics, University of New Mexico, Albuquerque NM 87109 USA.
3. Research School of Earth Sciences, Australian National University, Canberra ACT 0200 Australia.
4. Department of Chemistry, The University of Western Ontario, London ON N6A 5B7 Canada.
5. Pacific Northwest Consortium, Depts. of Physics, Simon Fraser University, Burnaby, BC, Canada and the University of Washington, Seattle, WA, USA.
6. Department of Earth & Environment, 50 College St, Mount Holyoke College, South Hadley MA 01075 USA.

ABSTRACT

Cerium L_3 absorption edge (L_3 – edge) X-ray Absorption Near Edge Structure (XANES) spectra were obtained from ~7 x 5 μm areas on green titanite and brown titanite (both with total Ce ~ 0.6 wt.%) using the X-ray microprobe at the Pacific Northwest Consortium – X-ray Science Division (PNC-XSD) Insertion Device (ID) line of the Advanced Photon Source (APS). Using a

wavelength dispersive X-ray (WDX) fluorescence detector with a bent LiF (220) crystal monochromator ($E/\Delta E \sim 1000$), we have overcome the challenge of having to measure trace amounts of Ce in a Ti-rich sample of which the energy of the fluorescence X-rays from Ce L_3 – edge and Ti K – edge excitation cannot be resolved with solid state detectors. We show that both Ce^{3+} and Ce^{4+} are present in our titanite samples by examining the Ce L_3 – edge XANES spectra.

Our results show that in order to correctly determine trace element substitution mechanisms in titanite (and other minerals) it is necessary to determine multivalent element concentrations, including Ce^{3+}/Ce^{4+}. We present a new approach for predicting and evaluating multivalent trace element substitution in titanite and other minerals.

Keywords: multivalent elements, XANES, trace element substitution

INTRODUCTION

Titanite ($CaTiSiO_5$, previously known as sphene) is a common mineral in mafic-felsic igneous and metamorphic rocks, and it is widely used for geochronologic and petrogenetic studies (Gromet and Silver, 1983; Green and Pearson, 1986; Wones, 1989; Xirouchakis and Lindsley, 1998; Frost et al., 2000; Piccoli et al., 2000; Xirouchakis et al., 2001a, b). A range of different major and trace elements are found in the titanite crystal lattice (Fig. 1) and, like other minerals, it is probable that titanite chemistry is related to the bulk composition of its host rock and intensive parameters during its crystallization. For instance, the Zr content of titanite has been related to pressure in experiments where titanite co-exists with quartz and rutile (Hayden et al., 2008).

Titanite commonly forms under relatively high oxygen fugacity (fO_2) conditions (Wones, 1989; Frost et al., 2000). It also contains several major elements that occur in multiple valences and may therefore be used as oxy-barometers including the major elements: Fe, Mn, and Ti. Chemical variations of Fe^{2+}/Fe^{3+} and Mn^{3+}/Mn^{4+} titanites have been considered with the tentative suggestion that the +3 valence state may dominate (e.g., Perseil and Smith, 1995), whereas Ti consistently occurs in the +4 valence state in terrestrial samples, even when metamict (Farges, 1997). In titanite, trace elements that occur in multiple valence states include Ce, Eu, Cr, and V. Because Ce^{4+} is a stronger oxidant than most commonly measured multivalent cations (e.g., Fe^{2+}/Fe^{3+}, Ti^{3+}/Ti^{4+}, Eu^{2+}/Eu^{3+}, V^{4+}/V^{5+}; Schreiber et al., 1987; Schreiber, 1987), the Ce valence state in titanites may record the relatively high fO_2 conditions common in ore deposits and volcanic rocks.

The potential usefulness of measuring Ce^{3+}/Ce^{4+} in titanite on a small spatial scale is constrained by analytical challenges. Since the Ti *K* absorption edge (*K* – edge; 4966 eV) is below the Ce L_3 absorption edge (L_3 – edge; 5723 eV), Ti $K\beta_{1,3}$ fluorescence line (4931 eV) will be present, and close in energy to the Ce $L\alpha_{1,2}$ fluorescence line (4840 eV) (Table 1). For low concentrations of cerium, the presence of a high Ti fluorescence contribution necessitates the use of detectors with high (a few eV) resolution. Of course, in natural samples, other elements may also be present, contributing additional nearby fluorescence emission.

Here, we apply the capability of tunable X-rays at a third-generation light source to determine Ce^{3+}/Ce^{4+} in titanite specimens using a micrometer-scale focused beam and X-ray Absorption Near-Edge Structure (XANES) spectroscopy. A wide range of multivalent elements have been analyzed in geologic materials using various XANES techniques (e.g., Fe^{2+}/Fe^{3+} - Bajt et al., 1994; Au^0/Au^+ - Cabri et al., 2000; Cr^{2+}/Cr^{3+} - Berry and O'Neill, 2004; $V^{2+}/V^{3+}/V^{4+}/V^{5+}$ -

Sutton et al., 2005). The study by Cabri et al. (2000) examined ppm-level gold valence (Au L_3 – edge = 11919 eV, $L\alpha$ = 9711 eV) in the presence of concentrated arsenic (As K = 11867 eV, $K\alpha$ = 10543 eV) and illustrates a similar challenge to dilute Ce in the presence of concentrated Ti – although those fluorescence X-ray peaks require less stringent separation they are complicated by the close proximity of the edge energies. Fortunately, in studying a dilute Ce/concentrated Ti system, the well-separated edge energies means little variation in Ti signal from the extended X-ray absorption fine structure (EXAFS) and an approach similar to Cabri et al. (2000) can be applied using a wavelength-dispersive X-ray detector (e.g., McKinley et al., 2004; Kaspar et al., 2006).

The Ce L_3 – edge XANES spectra of nominal Ce^{3+} ($4f^1$) and Ce^{4+} ($4f^0$) in the standards exhibit distinctly different features. Ce^{3+} shows a single white-line (sharp spike) arising from a $2p_{3/2}$ - $4d_{5/2,3/2}$ transition at the absorption threshold, whereas the Ce^{4+} spectrum shows a doublet. The doublet pattern is observed for compounds and complexes containing Ce^{4+} and the spectral features are recognized by many as the result of final state many-body effects (e.g., Sham et al., 2005). Ce^{3+} and Ce^{4+} L_3-edge XANES spectra are similar when the sample is in the solid state or in solution (e.g., Sham, 1989; Antonio and Soderholm, 1994) indicating that Ce^{3+} and Ce^{4+} may be determined quantitatively in minerals and composites. Furthermore, Takahashi et al. (2002) showed that Ce valence state determination by XANES is not affected by concentration, by examining spectra of Ce compounds that were diluted in silica.

In this paper, we make use of non-destructive methods for characterizing Ce in materials with high Ti concentrations on a small spatial scale (<10 μm across). We show that Ce^{3+}/Ce^{4+} may be detected in low concentrations in Ti-rich minerals. We also discuss the implications of a

range in Ce^{3+}/Ce^{4+} to trace element substitution in titanites, and model the role of multivalent elements on trace element substitutions.

METHODS

Major element analyses

Both green and brown titanites from a granodiorite pluton in North East Queensland, Australia (CMA-84-147) were obtained for this study. Major element compositions were determined using the JEOL JXA 8600 electron probe at The University of Western Ontario. We used a 15 kV accelerating voltage, and a 10 nA focused beam with wavelength dispersive spectroscopy and standard ZAF corrections.

Mössbauer analyses

To determine Fe^{2+}/Fe^{3+}, sample mounts were prepared for Mössbauer by gently crushing 7 and 10 mg of the brown and green titanite. Crystals were crushed under acetone, then mixing with a sugar-acetone solution designed to form sugar coatings around each grain and prevent preferred orientation. The amount of sample used was determined by the amount of sample available. Grains were gently heaped in a sample holder confined by Kapton tape. Mössbauer spectra were acquired at 295K using a source of ~50 mCi ^{57}Co in Rh on a WEB Research Co. model WT302 spectrometer (Mount Holyoke College). For each spectrum, the fraction of the baseline due to the Compton scattering of 122 keV gammas by electrons inside the detector was determined by measuring the count rate with and without a 14.4-keV stop filter (~2 mm of Al foil) in the gamma beam. Compton-corrected absorption was calculated for each individual spectrum using the formulation $A/(1 - b)$, where b is the Compton fraction and A is the uncorrected absorption. This correction does not change the results of the fits *per se* but does allow accurate determination of % absorption in the spectra. It is necessary because the range of

energy deposited in the detector by Compton events extends from 0 keV to 40 keV, overlapping both the 14 keV and 2 keV energies deposited by the 14 keV gammas.

Run times were 6-7 days for each spectrum due to low Fe contents, and baseline counts were 65 and 71 million after the Compton correction, as needed to obtain reasonable counting statistics on these very low Fe samples. Data were collected in 2048 channels and corrected for nonlinearity via interpolation to a linear velocity scale, which is defined by the spectrum of the 25 μm Fe foil used for calibration. Data were then folded before fitting, using a procedure that folds the spectrum about the channel value that produces the minimum least squares sum difference between the first half of the spectrum and the reflected second half of the spectrum.

Both spectra were processed using the MEX_FielDD program, which uses Lorentzian line shapes and solves full Hamiltonians for isomer shift and quadrupole splitting distributions in each of two valence states. Isomer shifts (δ), and quadrupole splittings (Δ) of the doublets were allowed to vary, and widths of peaks were allowed to vary in pairs.

Because the samples are low in iron and very small in mass, the Mössbauer spectra have less than ideal signal-to-noise ratios. Thus, errors on isomer shifts and quadrupole splitting are estimated at ±0.05-0.2 mm/s. The distribution of area between the two Fe^{3+} doublets is non-unique, and probably ±5-10% absolute, but the summed areas of the smaller (e.g. Fe^{3+}) components relative to the total area are accurate to within ±3-5% absolute.

Previous Mössbauer studies of titanite do not provide a clear consensus on the best way to model the data (Table 2). Many previous workers found a Fe^{3+} doublet with large quadrupole splitting (1.02-1.38 mm/s) indicative of a highly-distorted octahedral coordination polyhedron; this is assigned to Fe^{3+} in the TiO_6 polyhedra. A Fe^{3+} doublet with smaller Δ but widely-varying parameters are reported by Muir et al. (1984), Holényi and Annersten (1987), Niemeier et al.

(1999), and Vuorinen and Hålenius (2005); this feature was originally assigned by Muir et al. (1984) to the tetrahedral site but the more recent studies assigned it to both the tetrahedral site and the octahedral site in a different domain. Many workers observed a Fe^{2+} doublet with parameters of ~δ = 1.04-1.18 mm/s and Δ = 1.72-2.17 mm/s that also represents octahedral coordination.

XANES analyses

The Ce L_3 – edge XANES spectral measurements on standards and titanites were conducted at the PNC/XSD ID line (sector 20) at the Advanced Photon Source (APS), Argonne National Laboratory. The APS was operating in a 100 mA top-up mode (twenty 5 mA bunches, filled every 2 minutes). A cryogenic-cooled Si(111) double crystal monochromator (DCM) and Kirkpatrick-Baez (KB) mirrors were used to provide a monochromatic microbeam of ~7 μm (vertical) × ~5 μm (horizontal) for the measurement. The X-ray emission was analyzed with a wavelength dispersive X-ray (WDX) spectrometer using a bent LiF (220) crystal ($2d$ = 2.8473 Å) monochromator. We used a Microspec WDX-2A with a 25 um Kapton™ window aligned at 142° to the incident beam in the plane of the incident beam and linear polarization (electric field) vector. Reflected light optics were used to track the location of each analysis. A 13 element HPGe solid state detector (made by Canberra) was located at 90° to the incident beam in the direction of the polarization and was also used to monitor the fluorescence X-rays.

The DCM was calibrated at the K – edge of a Cr metal (5989.02 eV) and the LiF crystal was calibrated with the elastic peak. The best resolution from this crystal is ~ 5.5 eV at 4.8 keV. In the present study, the typical full width at half maximum of the Ce – $L\alpha_1$ peak was ~ 7 eV.

To determine the best energy range to monitor, we acquired a WDX scan with excitation energy above the Ce L_3 – edge of an available Ce intermetallic compound ($Ce_{25}Pd_{48}Sn_{27}$) that

was mounted as fine particles on tape in front of a Ti foil so that the small amount of transmission through the intermetallic allowed for some absorption and fluorescence yield from the Ti (Fig. 2a). We obtained another WDX scan in the same energy region for the green titanite that was prepared as a thin powder film on a carbon substrate (Fig. 2b).

The Ce fluorescence lines from the standard and the titanite appear at the same emission wavelength and the Ti $K\beta_{1,3}$ fluorescence ($M_{3,2}$ to K transition) from the green titanite sample is very close to the Ce $L\alpha$ lines. With the Ti concentration much higher than that for Ce, the integrated intensity under the Ti $K\beta_{1,3}$ peak is much larger (71 times more intense) than that of the Ce $L\alpha_1$ peak. The Ce $L\alpha$ lines were selected with the LiF (220) crystal for subsequent analyses of the absorption as a function of photon energy across the Ce L_3 – edge.

The titanite specimens were prepared as a thin powder film on a carbon substrate and a Ce map of the specimen was generated to help find areas with the highest concentration of Ce for microanalysis. The sample was analyzed in 20 μm steps in two-dimensions by mounting it on an *x*-*y* scanning stage with a mechanical stability of better than 100 nm. A fixed microbeam at energy above the Ce L_3 – edge threshold was used and the *x*-*y* plane of the sample stage was at a 45^{o} angle with respect to the incident X-ray photons and 142° to the WDX detector. The Ce $L\alpha$ emission map was then examined so that areas with higher absolute Ce concentrations could be analyzed to improve counting statistics; each spectrum reported comes from Ce-rich area that is ~7 x 5 μm.

The Ce L_3 – edge peak for the titanites was measured relative to a calibration based on commercial spectroscopic grade $CePO_4$ and CeO_2. The standards were prepared as fine powders (~1 μm) mounted on carbon tape and then scanned on the mapping stage to find a region of

uniform intensity. These compounds also provide the model Ce^{3+} and Ce^{4+} XANES spectra for analysis.

To process the spectra, all the edge jumps were normalized to unity. The height of the two peaks above the threshold in the titanite Ce L_3 – edge XANES spectra were then compared with the best fit of a simulation using the sum of the XANES of the $CePO_4$ and CeO_2. This criterion has the sensitivity of 1% beyond which mismatches become apparent by visual inspection.

It should be noted that while the XANES of $CePO_4$ may not be representative of a truly ionic Ce^{3+}, it is an appropriate choice for Ce^{3+} in an oxygen-rich environment like that found in titanite. This is demonstrated by examining the white line height relative to other Ce^{3+} compounds where the Ce is bonded to oxygen. The normalized intensity value ($I_{final}/I_{original}$) for $CePO_4$ is 2.69, $Ce_2Ti_2O_7$ is 2.19 (Gordon, unpublished data), $Ce_2(CO_3)_3.xH_2O$ is 2.32 (Jollivet et al., 2005) and $Ce_2(SO_4)_3$ is 2.37 (Curti et al., 2012). Taken together, these values have a standard deviation of less than 16% relative. Similarly, Takahashi et al. (2002; their Fig. 2) found a variation of less than 10% relative between the white line values for $Ce_2(CO_3)_3.xH_2O$, $Ce_2(SO_4)_3$, Ce(III)acetate and Ce(III)oxalate. Since the white line value for $CePO_4$ is at the high end of the range of values presented above, our use of it as a standard may have slightly underestimated the contribution of Ce^{3+} (<10% relative). However, this error is scalable; in other words, if we find that $CePO_4$ is not the best choice for a standard, our data may be scaled to another standard.

The choice of CeO_2 as a standard for the Ce^{4+} species is consistent with the procedures used by other workers (e.g., Curti et al., 2012; Jollivet et al., 2005; Overbury et al., 1998; Sham, 1989) and this is one of the most stable Ce-O compounds with consistent white line height. We note that Takahashi et al. (2002) used $Ce(SO_4)_2$ as a reference standard for the Ce^{4+} species;

however we avoided that compound due to its hygroscopic nature and because Ce-O-Ce bonds are a better analog for Ce-O-Si bonds in silicates (e.g., Curti et al., 2012).

Self-absorption effects may have occurred to some extent in the undiluted standards because the absorption length above the white line is ~ 5 μm, suggesting that the absorption length at the white line is ~1.5 - 2 μm. However, we did not observe any damping of the spectral features (below) that would be expected for self-absorption. Also, any self-absorption would tend to work in opposition to the effect where $CePO_4$ had a slightly higher white line than other standards (that also may suffer self-absorption effects). For the dilute samples, self-absorption is very unlikely.

RESULTS

Chemistry of the titanites

The green and brown titanite crystals have major element concentrations that are essentially within error of each other (Table 3). The green titanite has slightly higher concentrations of trace elements than the brown titanite (<10%; our unpublished data).

Mössbauer analyses

Results of the present study (Table 4) are similar to previous work (e.g., Muir et al. 1984; Holényi and Annersten, 1987; Niemeier et al., 1999; Vuorinen and Hålenius, 2005). Spectra of both brown and green titanite contain two Fe^{3+} doublets (Fig. 3). The doublet with the smaller Δ value is clearly tetrahedral because of its low δ value (0.15-0.16 mm/s). Our data also show a third doublet assigned to Fe^{2+} in octahedral coordination, but our observed values for Δ are slightly higher than those observed by previous workers. Repeated attempts to model these data with lower Δ values were made, but the upper velocity peak is clearly higher than those in other workers' data, even upon simple inspection. This difference could be the result of differing

degrees of metamictization, varying bulk compositions, high peak overlap of the lower-velocity Fe^{2+} peak with the Fe^{3+} peaks, or poor resolution due to low signal-to-noise. Both the brown and green titanites have the same amount of Fe^{2+} overall, which is 14% of the total iron.

Micro-XANES analyses

To find the areas with the highest concentration of Ce, for the best analysis, we mapped the grains mounted on carbon tape. Figure 4a shows a Ce concentration map of the green titanite specimen monitored with the Ce $L_{\alpha 1}$ emission. The map exhibits variations in the Ce fluorescence intensity that could be due to variations in particle geometry (thickness or orientation relative to the detector versus the beam spot) or in Ce concentration. The micro-XANES spectral patterns on single spots (~7 x 5 μm) in both high and intermediate intensity regions are identical except for the intensity, which is proportional to the Ce concentration (Figure 5b). This result indicates that the valence state of Ce is the same at these spots (within one particle) and is likely the same throughout the specimen despite the variation in absolute Ce concentration. Similar analysis was carried out for the brown titanite.

The Ce L_3 – edge XANES spectra of high Ce concentration areas of the brown and the green titanite, $CePO_4$ and CeO_2 are shown in Figure 5a-c. The Ce L_3 – edge XANES spectra for the green titanite is best represented by 71% Ce^{3+} and 29% Ce^{4+} based on the peak heights from the model compounds ($Ce^{3+}/Ce^{4+} = 2.45$). The brown titanite is best represented by 46% Ce^{3+} and 54% Ce^{4+} ($Ce^{3+}/Ce^{4+} = 0.85$).

Based on our estimate of the variation in Ce white line height amongst the Ce^{3+} standards the absolute values for the Ce^{3+}/Ce^{4+} may need to be adjusted (<16% relative) if we have chosen an inappropriate standard (e.g., $CePO_4$). The precision error is <10% relative based on fitting using a range of fit parameters.

DISCUSSION

Our study shows that Ce valence state may be measured on the micro-scale (<10 μm across) in Ti-rich materials where the Ce is bonded to oxygen, such as titanite. We have demonstrated that high resolution mapping for Ce^{3+}/Ce^{4+} is possible in silicate minerals with high Ti content. Our results are supported by Resonant Inelastic X-ray Scattering (RIXS) analyses of the green titanite presented in the Supplementary Material.

Because grain mounts or powders were used and mapped over a range of crystallographic orientations, our study avoided effects of crystallographic orientation on the Ce^{3+}/Ce^{4+} measurements of titanite (which is monoclinic, prismatic, and in the $P2_1/a$ space group). We note that Fe^{2+}/Fe^{3+} XANES studies show that such an effect exists in other minerals where Fe is a major element (Dyar et al., 2002), but V is not affected by crystallographic orientation in olivine (Sutton and Newville, 2005). Future analyses of Ce^{3+}/Ce^{4+} in minerals will need to consider crystallographic effects if single crystals or thin sections are used.

Trace element substitutions in titanites

Our data indicate that the green titanite shows a significant enrichment in Ce^{3+} (71%) relative to the brown titanite (46%), but the Fe^{3+}/Fe_{total} is the same in both minerals. Because multivalent element substitution may be important in understanding the trace element budget in titanite and other minerals, we now investigate the possible substitutions in detail.

Redox substitutions

The different Ce^{3+}/Ce^{4+} values may suggest that other redox couples are operating following:

$$^{VI}Ce^{4+} + {}^{VI}J^{n+} = {}^{VI}Ce^{3+} + {}^{VI}J^{(n+1)+} \quad (1)$$

where *J* is a multivalent element with a charge of n+ and (n+1)+ and the VI-fold crystallographic site is denoted by a superscript.

$^{VII}Ce^{3+}$ substitutions

Another possibility is that Ce^{3+} and Ce^{4+} act independently of each other. For instance, $^{VII}Ce^{3+}$ may play an important role, as proposed by many authors, and there may be substitutions between the VII-fold and VI-fold sites (Exley, 1980; Green and Pearson, 1986; Oberti et al., 1991; Piccoli et al., 2000; Russell et al., 1994; Tiepolo et al., 2002; Siefert and Kramer, 2003). These substitutions have the general form:

$$^{VII}Ce^{3+} + {}^{VI}X^{5+,\,4+,\,3+} = {}^{VII}Y^{3+,\,2+,\,1+} + {}^{VI}Z^{5+,\,4+,\,3+} \quad (2)$$

where *X, Y* and *Z* are different elements in the VI-fold and VII-fold sites, and the sum of the charge on Ce^{3+} + *X* equals the sum of the charge on *Y* + *Z*.

$^{VI}Ce^{3+,\,4+}$ substitutions

Alternately, Ce in VI-fold co-ordination may substitute for other VI-fold elements like Zr^{4+}. Such a substitution is most likely in titanites rich in 4+ trace elements like Zr-rich titanites (e.g., Chakhmouradian, 2004) and would follow the form:

$$^{VI}Ce^{3+,\,4+} + {}^{VI}G^{4+,\,5+} = {}^{VI}H^{3+,\,4+} + {}^{VI}K^{4+,\,5+} \quad (3)$$

where *G, H* and *K* are different elements in the VI-fold site, and the sum of the charge on $Ce^{3+,\,4+}$ + *G* equals the sum of the charge on *H*+ *K*.

The lattice strain model for understanding trace element substitution

The lattice strain model of Brice (1975) assumes that the cations are incorporated into a lattice site by displacing the surrounding atoms results in a change in the elastic strain energy, ΔG_{strain} following:

$$\Delta G_{strain} = 4\pi E N_A \left[\frac{r_0}{2}(r_i - r_0)^2 + \frac{1}{3}(r_i - r_0)^3\right] \quad (4)$$

Where E is the Young's modulus of the site, N_A is Avogadro's number, r_0 is the radius of the crystallographic site, and r_i is the radius of the substituent cation. This equation has been linked to trace element partition coefficients between a mineral and melt by Blundy and Wood (1994) using the observation by Onuma et al. (1968) that partition coefficients for isovalent cations show near-parabolic dependence on cation radius.

The lattice strain model emphasizes the importance of both E (which is constant for a particular crystallographic site) and $r_i - r_o$; however, it is limited to one crystallographic site and isovalent cations. Instead, many minerals have multivalent cation substitution on multiple crystallographic sites. Below, we investigate substitution on multiple crystallographic sites using the $r_i - r_o$ variable and valence state in the context of titanite; although our approach may be used for all minerals.

A new method for evaluating multi-site, multivalent trace element substitutions

To evaluate which of the multi-site and multivalent substitutions (1-3) is most important in titanites and which elements are involved, we have taken a simple approach of examining the ionic radii ($r_i - r_o$) versus valence. We allow cations with different ionic radii (r_1, r_2, r_3, and r_4) and differing valence to substitute on the VI- and VII-fold sites using radii from Shannon and Prewit (1969), supplemented by data in Dyar et al. (2007). We then aim to minimize strain in the titanite crystal, by finding the substitutions that minimize the overall change in ionic radii versus valence. This can be illustrated by examining the coupled substitution on two crystallographic sites using a graph of ionic radii versus valence. For example, Figure 6 shows a substitution following:

$$^{x}A^{n+} + {}^{y}D^{(n+2)+} = {}^{x}B^{(n+1)+} + {}^{y}C^{(n+1)+} \quad (5)$$

where x and y are crystallographic sites and cations *A, B, C* and *D* have radii of r_a, r_b, r_c, and r_d respectively and *n* is a positive integer. We argue that substitutions like substitution 5 are favorable because the overall change in combined ionic radii and valence is minimized. Such a substitution produces a parallelogram in Figure 6 with the slope of line $AB = (r_b - r_a)/(1)$. This slope should be the same as the slope for line $CD = (r_d - r_c)/(1)$. We will refer to these lines as *line pairs*. Also, the slope of *AC* = slope of *BD* in Figure 6.

In contrast, less favorable substitutions have significant differences in the overall change in combined ionic radii and valence, and these substitutions are described by trapezoids (trapeziums) where the line pairs do not have the same slope. An example of such a substitution, shown in Figure 6, is:

$$^{x}A^{n+} + {}^{y}F^{(n+2)+} = {}^{x}B^{(n+1)+} + {}^{y}E^{(n+1)+} \quad (6)$$

and for this substitution, the slopes of lines $AB \neq EF$ and $AE \neq BF$. Substitutions with a greater mismatch between their slopes will be more unfavorable.

Our approach is simple and based on ionic radii and charge as the two main controls on trace element partitioning, like Goldschmidt's rules (Goldschmidt, 1937). However, there are some important caveats when using the method: 1) it does not take into account other factors such as electronegativity (Ringwood, 1955) and is not strictly based on thermodynamic or bonding processes (cf. Burns and Fyfe, 1967; Brice, 1974); 2) only cations that realistically substitute on the particular sites should be examined; 3) the method has not been developed for materials that contain substitutions with vacant sites, multiple substitution on one site (e.g., $^{VII}Ce^{3+} + {}^{VII}Na^{+} = 2\,{}^{VII}Ca^{2+}$) nor with anions. Next we apply this method to titanite substitutions with Ce^{3+} and Ce^{4+}.

348 *Examination of redox substitutions*

349 Possible redox couples with $^{VI}Ce^{3+}/^{VI}Ce^{4+}$ in the titanite are shown in Figure 7 and
350 include $^{VI}Mn^{3+}/^{VI}Mn^{4+}$, $^{VI}V^{3+}/^{VI}V^{4+}$, $^{VI}V^{4+}/^{VI}V^{5+}$, or ($^{VI}Nb^{4+}$, $^{VI}Ta^{4+}$)/($^{VI}Nb^{5+}$, $^{VI}Ta^{5+}$).
351 Additionally, $^{VI}Fe^{2+}/^{VI}Fe^{3+}$ and $^{VI}Mn^{2+}/^{VI}Mn^{3+}$ may act as redox couples although the 2+ cations
352 are less favored on the VI-fold site.

353 In Table 5, we give the slopes for the line pairs involved in the substitutions. Note that
354 $^{VI}Fe^{2+}/^{VI}Fe^{3+}$ and $^{VI}Mn^{3+}/^{VI}Mn^{4+}$ have near-parallelogram slopes with $^{VI}Ce^{3+}/^{VI}Ce^{4+}$, whereas the
355 other substitutions form trapezoidal shapes or have a large difference within the line slope pairs
356 (e.g. >0.06). Based on the difference in line pair slopes, the most likely substitutions are:

357 $$^{VI}Ce^{4+} + {}^{VI}Fe^{2+} = {}^{VI}Ce^{3+} + {}^{VI}Fe^{3+} \quad (7)$$

358 and

359 $$^{VI}Ce^{4+} + {}^{VI}Mn^{3+} = {}^{VI}Ce^{3+} + {}^{VI}Mn^{4+} \quad (8)$$

360 However, substitution 7 may be ruled out because 1) Fe^{2+} is not favored on the VI-fold
361 site in titanite; and 2) for the green and brown titanites, the bulk Fe^{3+} is the same (86% of total
362 Fe; Table 3). This suggests that $^{VI}Fe^{2+}/^{VI}Fe^{3+}$ may play a minor role in coupled substitutions
363 with $^{VI}Ce^{3+}/^{VI}Ce^{4+}$ in these titanites, unlike other Fe-rich systems (e.g., Schreiber et al., 1987;
364 Schreiber, 1987).

365 Substitution 8 where Ce is coupled with Mn^{3+}/Mn^{4+} is possible and different valences of
366 Mn may account for the color differences. But, further analyses of Mn-valence state are needed
367 to test this hypothesis because Mn^{4+} is uncommon in silicate minerals. Another Mn redox couple
368 is possible:

369 $$^{VI}Ce^{4+} + {}^{VI}Mn^{2+} = {}^{VI}Ce^{3+} + {}^{VI}Mn^{3+} \quad (9)$$

However, Mn^{2+} is not favored on the VI-fold site; therefore, although this method predicts that the difference between the slopes for the line pairs is low (Table 5), the redox substitution with Mn^{2+}/Mn^{3+} is unlikely.

Redox substitutions with Cr^{3+}/Cr^{4+}, V^{3+}/V^{4+}, V^{4+}/V^{5+} and $(Nb,Ta)^{4+}/(Nb,Ta)^{5+}$ are also shown in Table 5 and Figure 7b. These substitutions are also possible, but are less favored due to larger values of slope differences.

Examination of $^{VII}Ce^{3+}$ substitutions

Substitutions involving $^{VII}Ce^{3+}$ exchange with $^{VII}Ca^{2+}$ have been proposed for many titanites because the $^{VII}Ca^{2+}$ ion has an ionic radius of 1.06 Å which is similar to $^{VII}Ce^{3+}$ with an ionic radius of 1.07 Å (Shannon and Prewitt,1969). Ca is the most favorable element in the VII-fold site for Ce^{3+} substitution based on partitioning data (Tiepolo et al., 2002).

We evaluated all possible substitutions that create a parallelogram shape and have low line slope differences and found the following substitutions with decreasing likelihood (Table 5):

$$^{VII}Ce^{3+} + {}^{VI}Ti^{4+} = {}^{VII}Ca^{2+} + {}^{VI}(Nb,Ta)^{5+} \quad (10)$$

$$^{VII}Ce^{3+} + {}^{VI}Al^{3+} = {}^{VII}Ca^{2+} + {}^{VI}Ti^{4+} \quad (11)$$

$$^{VII}Ce^{3+} + {}^{VI}V^{3+} = {}^{VII}Ca^{2+} + {}^{VI}Ti^{4+} \quad (12)$$

$$^{VII}Ce^{3+} + {}^{VI}(Mn, Fe)^{3+} = {}^{VII}Ca^{2+} + {}^{VI}Ti^{4+} \quad (13)$$

We ignored possible substitutions with Ti^{3+} because it has not been observed in titanites.

Interestingly, our new approach shows that some substitutions involving both $^{VII}Ce^{3+}$ and $^{VII}Ca^{2+}$ and proposed in the literature form trapezoid shapes or lines and are therefore not favored using this model. For example:

$$2\,{}^{VII}Ce^{3+} + {}^{VI}Fe^{2+} = 2\,{}^{VII}Ca^{2+} + {}^{VI}Ti^{4+} \quad (14)$$

Examination of $^{VI}Ce^{3+, 4+}$ substitutions

Finally, we also evaluated substitutions in the VI-fold site for both $^{VI}Ce^{3+}$ and $^{VI}Ce^{4+}$ (substitution 4). The substitutions with parallelogram shapes on an ionic radii versus valence diagram include:

$$^{VI}Ce^{4+} + {}^{VI}(Nb, Ta)^{4+} = {}^{VI}Ce^{3+} + {}^{VI}V^{5+} \quad (15)$$

$$^{VI}Ce^{4+} + {}^{VI}Zr^{4+} = {}^{VI}Eu^{3+} + {}^{VI}(Nb, Ta)^{5+} \quad (16)$$

Despite the low difference between the line slope values for these reactions (Table 5), both are unlikely except where the concentrations of those trace elements are high.

Substitutions in the green and brown titanites

Our graphical method for predicting substitutions shows that in order to understand the origin of the Ce^{3+}/Ce^{4+} differences in the green and brown titanites it is necessary to collect data for other multivalent elements such as Fe, Mn, Cr, V, Nb and Ta (Table 4). Most favorable substitutions involving Ce^{3+} and/or Ce^{4+} include another multivalent element (e.g., substitution 7-10 and 12-16).

Several lines of evidence suggest that $^{VI}Mn^{3+}/^{VI}Mn^{4+}$ should be investigated further for its role as a redox couple with $^{VI}Ce^{3+}/^{VI}Ce^{4+}$. First, the Mn redox couple forms a parallelogram on an ionic radii versus valence diagram. Second, the other multivalent elements form trapezoid shapes on such diagrams or are involved in more complicated substitutions that involve multiple elements and/or crystallographic sites. Third, the green versus brown color possibly suggests a difference in the concentration of a multivalent transition element; Mn is reasonably abundant and Fe is ruled out because Fe^{2+}/Fe^{3+} is the same in both crystals (86%). Currently, there are no measurements, to our knowledge, of the valence state of Mn in titanites to support this substitution one way or the other. Measurement of Mn valence state is an area of future research in silicate minerals from highly oxidized environments.

While it is not the aim of this study to determine the origin of the Ce^{3+}/Ce^{4+} values, it is possible that the green versus brown titanites formed under either different local fO_2 conditions, perhaps related to magma influx, crystallization or degassing. Alternately, the different titanites may have formed at different temperatures or from different melt compositions, like proposed for zoned titanites in other granites (McLeod et al., 2011). Finally, the different mineral colors and Ce^{3+}/Ce^{4+} values may result from metamictization (radiation damage; e.g., from U or Th).

RECOMMENDATIONS FOR FUTURE WORK

We have established a methodology for the micro-analysis of Ce^{3+}/Ce^{4+} in Ti-rich minerals using synchrotron XANES spectroscopy and a WDX detector. This technique is greatly facilitated by the stability of a third generation light source (APS). The XANES technique provides a methodology by which Ce^{3+}/Ce^{4+} in Ti-rich materials can be determined. The recently developed Minixs high energy resolution X-ray fluorescence analyzer, which uses flat crystals in a quasi-Johann or von Hamos arrangement in conjunction with a two-dimensional position-sensitive detector to measure a range of emission energies for a given incident energy, will greatly facilitate this kind of analysis in the future (Dickinson et al., 2008; Mattern et al., 2012).

This study shows that in order to understand trace element substitutions in titanite (and other minerals) it is critical to know Ce^{3+}/Ce^{4+} as well as the valence state of other multivalent elements. Our graphical analysis method indicates that the most favorable substitutions with Ce ions involve other multivalent ions. Therefore, to properly understand trace element substitution and to test our graphical technique it is necessary to measure multivalent elements, particularly Mn valence state. Finally, our approach for predicting and evaluating trace element substitutions in titanite may be applied to other minerals.

Titanite has great potential as an fO_2 sensor in natural rocks once it has been calibrated experimentally (e.g., like Kress and Carmichael, 1988; Carmichael, 1991; Canil et al., 1994; King et al., 2002; Berry and O'Neill, 2004; Sutton et al., 2005). Another advantage of titanite is that it may be dated and therefore used to examine fO_2 changes over time. However, to use titanite and other minerals for this purpose it is necessary to understand the likely multivalent substitutions.

ACKNOWLEDGEMENTS

We are grateful to Charlotte Allen, Australian National University, for providing the two titanite specimens. Steve Sutton and Richard Hervig are thanked for helpful conversations. Two anonymous reviewers provided helpful comments. PLK and TKS were supported by grants from NSERC. The PNC-CAT at APS was supported by US Department of Energy and an NSERC MFA grant to Simon Fraser University.

REFERENCES

Antonio, M. and Soderholm, L. (1994) Cerium valence in cerium-exchanged Preyssler's heteropolyanion through X-ray Absorption Near-Edge Structure. Inorganic Chemistry, 33, 5988-5993.

Aramu, F., Brovetto, P., Delunas, A., Maxia, V., and Rinaldi R. (1990) Mössbauer spectroscopy of a natural titanite. Il Nuovo cimento della Societa itliana di fisica. D., 12, 133-138.

Bajt, S., Sutton, S.R., and Delaney, J.S. (1994) X-ray microprobe analysis of iron oxidation states in silicates and oxides using X-ray absorption near edge structure (XANES). Geochimica et Cosmochimica Acta, 58, 5209-5214.

Berry, A.J., and O'Neill, H.S.C. (2004) A XANES determination of the oxidation state of chromium in silicate glasses. American Mineralogist, 89, 790-798.

463 Blundy, J. D. and Wood, B. J. (1994) Prediction of crystal-melt partition coefficients from elastic
464 moduli. Nature, 372, 452-454.
465 Brice, J.C. (1975) Some thermodynamic aspects of the growth of strained crystals. Journal of
466 Crystal Growth, 28, 249-253.
467 Burns, R.G. (1993) Mineralogical Applications of Crystal Field Theory (Second edition). 576 p.
468 Cambridge Univ. Press, Cambridge, UK.
469 Burns, R.G. and Fyfe, W.S. (1967) Trace element distribution rules and their significance.
470 Chemical Geology, 2, 89-104.
471 Cabri, L.J., Newville, M., Gordon, R.A., Crozier, E.D., Sutton, S.R., McMahon, G., and Jiang,
472 D.-T., (2000) Chemical speciation of gold in arsenopyrite. Canadian Mineralogist, 38,
473 1265-1281.
474 Canil, D., O'Neill, H.S.C., Pearson, D.G., Rudnick, R.L., McDonough, W.F., and Carswell, D.A.
475 (1994) Ferric iron in peridotites and mantle oxidation states. Earth and Planetary Science
476 Letters, 123, 205-220.
477 Carmichael, I.S.E. (1991) The redox state of basic and silicic magmas: a reflection of their
478 source regions? Contributions to Mineralogy and Petrology 106, 129-141.
479 Chakhmouradian, A.R. (2004) Crystal chemistry and paragenesis of compositionally unique
480 (Al-, Fe-, Nb-, and Zr-rich) titanite from Afrikanda, Russia. American Mineralogist, 89,
481 1752–1762.
482 Curti, E., Grolimund, D., and Borca, C.N. (2012) A micro-XAS/XRF and thermodynamic study
483 of $Ce^{III/IV}$ speciation after long-term aqueous alteration of simulated nuclear waste glass:
484 Relevance for predicting Pu behavior? Applied Geochemistry, 27, 56-63.

485 Dickinson, B., Seidler, G.T., Webb, Z.W., Bradley, J.A., Nagle, K.P., Heald, S.M., Gordon,
486 R.A., and Chou, I.M. (2008) A short working distance multiple crystal X-ray
487 spectrometer, Review of Scientific Instruments, 79, 123112, doi:10.1063/1.3048544.
488 Dyar, M.D., Gunther, M.E., and Tasa, D. (2007) Mineralogy and Optical Mineralogy. 708 p.
489 Mineralogical Society of America, Chantilly, VA, USA.
490 Dyar, M.D., Gunter, M.E., Delaney, J.S., Lanzarotti, A., and Sutton, S.R. (2002) Systematics in
491 the structure, optical properties, and XANES spectra of pyroxenes, amphiboles, and
492 micas. Canadian Mineralogist, 40, 1375-1393.
493 Exley, R.A. (1980) Microprobe studies of REE-rich accessory minerals: implications for Skye
494 granite petrogenesis and REE mobility in hydrothermal systems. Earth and Planetary
495 Science Letters, 48, 97–110.
496 Farges, F. (1997) Fivefold-coordinated Ti^{4+} in metamict zirconolite and titanite: A new
497 occurrence shown by Ti K-edge XANES spectroscopy. American Mineralogist, 82, 44-
498 50.
499 Frost, B.R., Chamberlain, K.R., and Schumacher, J.C. (2000) Sphene (titanite): phase relations
500 and role as a geochronometer. Chemical Geology, 172, 131-148.
501 Goldschmidt, V.M. (1937) The principles of distribution of chemical elements in minerals and
502 rocks. Journal of the Chemical Society, 1937, 655-672.
503 Green, T.H. and Pearson, N.J. (1986) Rare-earth element partitioning between sphene and
504 silicate liquid at high pressure and temperature. Chemical Geology, 55, 105-119.
505 Gromet, L.P. and Silver, L.T. (1983) Rare earth element distributions among minerals in a
506 granodiorite and their petrogenetic implications. Geochimica et Cosmochimica Acta, 47,
507 925-939.

508 Hawthorne, F.C., Groat, L.A., Raudsepp, M., Ball, N.A., Kimata, M., Spike, F.D., Gaba, R.,
509 Halden, N.M., Lumpkin, G.R, Ewing, R.C., Greegor, R.B., Lytle, F.W., Ercit, T.S.,
510 Rossman, G.R., Wicks, F.J., Ramik, R.A., Sherriff, B.L., Fleet, M.E., and McCammon,
511 C. (1991) Alpha-decay damage in titanite. American Mineralogist, 76, 370-396.
512 Hayden, L.A., Watson, E.B., and Wark, D.A. (2008) A thermobarometer for sphene (titanite).
513 Contributions to Mineralogy and Petrology, 155, 529-540, DOI: 10.1007/s00410-007-
514 0256-y
515 Higgins, J.B. and Ribbe, P.H. (1976) The crystal chemistry and space groups of natural and
516 synthetic titanites. American Mineralogist, 61, 878-888.
517 Holényi, K. and Annersten, H. (1987) Iron in titanite: A Mössbauer spectroscopy study.
518 Canadian Mineralogist, 25, 429-433.
519 Huges, J.M., Bloodaxe, E.S., Hanchar, J.M., and Foord, E.E. (1997) Incorporation of rare earth
520 elements in titanite: stabilization of the A2/a dimorph by creation of antiphase
521 boundaries. American Mineralogist, 82, 512-516.
522 Jollivet, P., Lopez, C., Den Auwer, C., and Simoni, E. (2005) Evolution of the local environment
523 of cerium and neodymium during simplified SON68 glass alteration. Journal of Nuclear
524 Materials, 346, 253-265.
525 Kaspar, T. C., Droubay, T., Shutthanandan, V., Heald, S. M., Wang, C. M., McCready, D. E.,
526 Thevuthasan, S., Bryan, J. D., Gamelin, D. R., Kellock, A. J., Toney, M. F., Hong, X.,
527 Ahn, C. H., and Chambers, S. A. (2006) Ferromagnetism and structure of epitaxial Cr-
528 doped anatase TiO_2 thin films. Physical Review B, 73, 155327.

King, P.L., Hervig, R.L., Holloway, J.R., Delaney, J.S., and Dyar, M.D. (2000) Fe^{3+}/Fe_{total} and H partitioning between amphiboles and basanitic melts as a function of oxygen fugacity. Earth and Planetary Science Letters, 178, 97-112.

Kress, V.C. and Carmichael, I.S.E. (1988) Stoichiometry of the iron oxidation reaction in silicate melts. American Mineralogist, 73, 1267-1274.

Mattern, B.A., Seidler, G.T., Haave, M., Pacold, J.I., Gordon, R.A., Planillo, J., Quintana, J. and Rusthoven, B. (2012) A plastic miniature x-ray emission spectrometer based on the cylindrical von Hamos geometry. Reviews Scientific Instruments, 83, 023901, DOI: 10.1063/1.3680598

McLeod, G.W., Dempster, T.J., and Faithfull, J.W. (2011) Deciphering magma-mixing processes using zoned titanite from the Ross of Mull Granite, Scotland. Journal of Petrology, 52, 55-82. doi: 10.1093/petrology/egq071.

McKinley, J.P., Zachara, J.M., Heald, S.M., Dohnalkova, A., Newville, M.G., and Sutton, S.R. (2004) Microscale distribution of cesium sorbed to biotite and muscovite. Environmental Science Technology, 38, 1017-1023.

Muir, I.J., Metson, J.B., and Bancroft, M. (1984) ^{57}Fe Mössbauer spectroscopy of perovskite and titanite. Canadian Mineralogist, 22, 689-694.

Niemeier, D., Mehner, H., Bismayer, U., and Becker, K.D. (1999) A temperature-dependent ^{119}Sn and ^{57}Fe Mössbauer study of malayaite, $CaSnSiO_5$:Fe. Physica Status Solidi, 211, 581-594.

Oberti, R., Smith, D.C., Rossi, G., and Caucia, F. (1991) The crystal-chemistry of high-aluminum titanites. European Journal of Mineralogy, 3, 777-792.

551 Onuma, N., Higuchi, H., Wakita, H., and Nagasawa, H. (1968) Trace element partitioning
552 between two pyroxenes and the host lava. Earth and Planetary Science Letters, 5, 47-51.
553 Overbury, S.H., Huntley, D.R., Mullins, D.R., and Glavee, G.N. (1998) XANES studies of the
554 reduction behavior of $(Ce_{1-y}\ Zr_y)O_2$ and $Rh/(Ce_{1-y}\ Zr_y)O_2$. Catalysis Letters, 51, 133-138.
555 Perseil, E.A. and Smith, D. (1995) Sb-rich titanite in the manganese concentrations at St. Marcel-
556 Praborna, Aosta Valley, Italy: petrography and crystal chemistry. Mineralogical
557 Magazine, 59, 717-734.
558 Piccoli, P., Candela, P., and Rivers, M. (2000) Interpreting magmatic processes from accessory
559 phases: titanite - a small-scale recorder of large-scale processes. Transactions of the
560 Royal Society of Edinburgh - Earth Sciences, 91, 257-267.
561 Ribbe, P.H. (1980) Titanite. In P.H. Ribbe, ed. Orthosilicates, 5, p. 137-154. Reviews in
562 Mineralogy, Mineralogical Society of America, Blacksburg, Virginia.
563 Ringwood, A.E. (1955) The principles governing trace element distribution during magmatic
564 crystallization Part I: The influence of electronegativity. Geochimica et Cosmochimica
565 Acta, 7, 189-202.
566 Russell, J.K., Groat, L.A., and Halleran, A.D. (1994) LREE-rich niobian titanite from Mount
567 Bisson, British Columbia: Chemistry and exchange mechanisms. Canadian Mineralogist,
568 32, 575-587.
569 Schreiber, H. D. (1987) An electrochemical series of redox couples in silicate melts: A review
570 and applications to geochemistry. Journal of Geophysical Research, 92, 9225-9232.
571 Schreiber, H. D., Merkel Jr., R. C., Schreiber, V. L., and Balazs, G. B. (1987) Mutual
572 interactions of redox couples via electron exchange in silicate melts: Models for
573 geochemical melt systems. Journal of Geophysical Research, 92, 9233-9245.

574 Sham, T.K. (1989) Electronic structure of hydrated Ce^{4+} ions in solution: An x-ray absorption
575 study. Physical Review, B40, 6045-6051.
576 Sham, T.K., Gordon, R.A., and Heald, S.M. (2005) Resonant inelastic scattering at the Ce L_3
577 edge of $CePO_4$ and CeO_2: implications for the valence of CeO_2 and related phenomena.
578 Physical Review, B72, 035113 (1-6).
579 Shannon, R.D. and Prewitt, C.T. (1969) Effective ionic radii in oxides and fluorides. Acta
580 Crystallographica, B25, 925-946.
581 Siefert, W. and Kramer, W. (2003) Accessory titanite: an important carrier of zirconium in
582 lamprophyres. Lithos, 71, 81-98.
583 Sutton, S.R. and Newville, M. (2005) Vanadium K XANES of synthetic olivine: Valence
584 determinations and crystal orientation effects. Lunar and Planetary Science Conference,
585 36^{th}, Abstract #2133.
586 Sutton, S.R., Karner, J., Papike, J., Delaney, J.S., Shearer, C., Newville, M., Eng, P., Rivers, M.,
587 and Dyar, M.D. (2005) Vanadium K edge XANES of synthetic and natural basaltic
588 glasses and application to microscale oxygen barometry. Geochimica et Cosmochimica
589 Acta, 69, 2333-2348.
590 Takahashi, Y., Sakami, H., and Nomura, M. (2002) Determination of the oxidation state of
591 cerium in rocks by Ce L_{III}-edge X-ray absorption near-edge structure spectroscopy.
592 Analytica Chimica Acta, 468, 345-354.
593 Thompson, A. and 13 others. (2001) X-Ray Data Booklet. 457 p. Center for X-ray Optics and
594 Advanced Light Source, Lawrence Berkeley National Laboratory, Berkeley, California.

595 Tiepolo, M., Oberti, R., and Vannucci, R. (2002) Trace-element incorporation in titanite:
596 constraints from experimentally determined solid/liquid partition coefficients. Chemical
597 Geology, 191, 105-119.
598 Vuorinen, J.H. and Hålenius, U. (2005) Nb-, Zr-, and LREE-rich titanite from the Alnö alkaline
599 complex: Crystal chemistry and its importance as a petrogenetic indicator. Lithos, 83,
600 128-142.
601 Wones, D.R. (1989) Significance of the assemblage titanite + magnetite + quartz in granitic
602 rocks. American Mineralogist, 74, 744-749.
603 Xirouchakis, D. and Lindsley, D.H. (1998) Equilibria among titanite, hedenbergite, fayalite,
604 quartz, ilmenite, and magnetite: Experiments and internally consistent thermodynamic
605 data for titanite. American Mineralogist, 83, 712-725.
606 Xirouchakis, D., Lindsley, D.H., and Andersen, D.J. (2001a) Assemblages with titanite
607 ($CaTiOSiO_4$), Ca-Mg-Fe olivine and pyroxenes, Fe-Mg-Ti oxides, and quartz: Part 1.
608 Theory. American Mineralogist, 86, 247-253.
609 Xirouchakis, D., Lindsley, D.H., and Andersen, D.J. (2001b) Assemblages with titanite
610 ($CaTiOSiO_4$), Ca-Mg-Fe olivine and pyroxenes, Fe-Mg-Ti oxides, and quartz: Part II.
611 Application. American Mineralogist, 86, 254-264.
612

Figure Captions

FIGURE 1: Portion of the titanite structure showing the edge-sharing octahedral and corner-sharing tetrahedral surrounding the VII-coordinated site where Ce resides (mid gray). The octahedra form kinked corner-sharing chains that are cross-linked by the SiO_4 tetrahedra (dark gray). Each tetrahedron shares O^{2-} with four separate octahedra (VI-fold, light gray) in three different chains, and that framework encloses the VII-coordinated site (mid gray). The octahedral sites are commonly filled with $Ti^{4+}O_6$ but may also contain Al, Fe and high field strength elements as labeled (e.g., Zr, Nb and Y). Large irregular VII-fold polyhedra (mid-grey) are dominated by CaO_7 (Ca in large circle) and also host other large ions including Ce and other REE, U, Th and Pb (Higgins and Ribbe, 1976; Huges et al., 1997), and Ba and Sr (Perseil and Smith, 1995). These VII-fold polyhedra form chains parallel to [101] that are connected by shared edges via O5 couples, thus any substitution in the VII-fold site can be charge-balanced by another substitution in any of the adjacent VI-, IV- or VII-fold sites (Tiepolo et al., 2002). In a 20-oxygen unit cell, one of the oxygen atoms, the underbonded O1 site (small circle), can be replaced by OH and F (Ribbe, 1980). Note that in metamict titanites, Ti^{4+} may be in V-fold co-ordination (Farges, 1997).

FIGURE 2: WDX scan (intensity versus emission wavelength) for (a) $Ce_{25}Pd_{48}Sn_{27}$ powder on a Ti substrate and (b) green titanite powder on a carbon substrate.

FIGURE 3: Mössbauer spectra of brown and green titanite. Data points are plotted a vertical black lines with magnitudes equal to the standard errors and the fit to the data is shown with the grey line. Fe^{2+} doublets are shown as solid black lines, and Fe^{3+} as dashed lines. Both these spectra have the same overall profile, though the two Fe^{3+} doublets exchange area between the two spectra. These differences represent subtle variations between distributions around the Fe^{3+}

636 cations. The area of the Fe^{2+} doublet in both spectra is the same, and thus it is inferred that the
637 two samples have identical $Fe^{3+}/\Sigma Fe$.

638 **FIGURE 4:** A) A Ce element map of the green titanite specimen monitored with the Ce $L\alpha_1$
639 emission. Each pixel is 20 x 20 μm. The intensity is color-coded such that the lighter color
640 pixels represent higher Ce concentration. Titanite grains of ~ 60 nm across and larger are clearly
641 visible on the black carbon tape background. B) Micro-XANES spectra from a ~7 x 5 μm area
642 obtained within a high and moderate intensity pixel.

643 **FIGURE 5:** Ce L_3 – edge XANES spectra of a) green titanite; b) brown titanite, and; c) $Ce^{3+}PO_4$
644 and $Ce^{4+}O_2$ compounds.

645 **FIGURE 6:** Diagram of ionic radii versus valence state illustrating the model for examining
646 favorable versus unfavorable substitutions. Favorable substitutions form parallelogram shapes,
647 whereas unfavorable form trapezoids.

648 **FIGURE 7:** Ionic radii versus valence diagram showing possible redox couple substitutions with
649 Ce^{3+} and Ce^{4+} in titanites. In the case of elements with high and low spin states we have used
650 ionic radii for the high spin state most common in nature (Burns, 1993). The ionic radii and
651 valences were taken from Shannon and Prewitt (1969), supplemented by a compilation in Dyar
652 et al. (2007). a) Based on the model, favorable substitutions show a near-parallelogram shape
653 and include: $^{VI}Ce^{4+} + {}^{VI}Fe^{2+} = {}^{VI}Ce^{3+} + {}^{VI}Fe^{3+}$ and $^{VI}Ce^{4+} + {}^{VI}Mn^{3+} = {}^{VI}Ce^{3+} + {}^{VI}Mn^{4+}$. b) Less
654 favorable substitutions show a trapezoid shape and include redox pairs with V.
655
656

657 **Table 1. Relevant X-ray energies for Ti and Ce**

Element	Absorption edge	X-ray fluorescence lines (relative intensity)*
Ti	K – edge: 4966 eV	$K\alpha_{1,2}$: 4510.8 eV/ 2.7486 Å (100) 4504.9 eV/ 2.7522 Å (50) $K\beta_{1,3}$: 4931.8 eV/ 2.5140Å (15)
Ce	L_3 – edge: 5723 eV	$L\alpha_{1,2}$: 4840.2 eV/ 2.5616 Å (100) 4823.0 eV/ 2.5707Å (11) $L\beta_1$: 5262.2 eV/ 2.356 Å (61)

658 * The fluorescence yield for Ti K – edge and Ce L_3 – edge X-rays are 0.214 and 0.111,
659 respectively (see text). Data is taken from Thompson et al. (2001).
660

661

Table 2. 295K Mössbauer parameters for titanite minerals in the literature

	Fe^{3+}		Fe^{2+}	
	δ (mm/s)	Δ (mm/s)	δ (mm/s)	Δ (mm/s)
Muir et al. (1984)	0.39-0.44	0.74-0.92	1.06-1.18	1.72-2.17
Holényi and Annersten (1987)	0.08	1.38		
	0.13	0.85		
	0.30	0.76		
Aramu et al. (1990)	0.38	1.31	1.07	2.00
Hawthorne et al. (1991)	0.33-0.38	1.02-1.27	1.04-1.12	2.09-2.16
Niemeier et al. (1999)	0.37	0.57		
	0.27	0.69		
	0.21	1.07		
	0.30	1.37		
Vuorinen and Hålenius (2005)	0.35-0.36	1.18-1.19	1.06-1.09	1.97-2.02
	0.68-0.70	0.56-0.52		

662

663 **Table 3. Average analyses of the brown and green titanites***

	Brown titanite			Green titanite		
	No.	*wt. %*	*1σ*	*No.*	*wt. %*	*1σ*
Major elements (Electron probe)						
SiO_2	19	29.67	0.23	14	29.58	0.20
TiO_2	19	36.27	0.58	14	36.85	0.42
Al_2O_3	19	1.23	0.17	14	1.08	0.07
Fe_2O_3	19	1.52	0.21	14	1.37	0.12
MnO	19	0.15	0.05	14	0.15	0.05
MgO	19	0.01	0.01	14	0.01	0.01
CaO	19	27.04	0.30	14	27.59	0.34
Na_2O	19	0.02	0.04	14	0.02	0.02
Ce^{4+} (XANES)		54%			29%	
Fe^{3+} (Mössbauer)		86%			86%	

664
665 * No. = number of analyses
666

667

Table 4. Mössbauer parameters for the brown and green titanites.

Assignment	Parameter	Brown	Green
$^{VI}Fe^{2+}$	δ (mm/s)	1.08	1.12
	Δ (mm/s)	2.46	2.57
	Γ (mm/s)	0.39	0.25
	% Area	14	14
$^{IV}Fe^{3+}$	δ (mm/s)	0.15	0.16
	Δ (mm/s)	0.61	0.65
	Γ (mm/s)	0.46	0.45
	% Area	23	59
$^{VI}Fe^{3+}$	δ (mm/s)	0.42	0.44
	Δ (mm/s)	1.14	1.20
	Γ (mm/s)	0.71	0.40
	% Area	63	28
	χ^2	0.61	0.56
	% Fe^{3+}	86	86

668
669

Table 5: Possible substitutions in titanite presented using the slopes (($r_i - r_o$)/ Δvalence) and line pair slope difference.

Substitution / couple	**Slope** **($r_i - r_o$)/ (Δvalence)**	**Line pair slope difference**	**Comments**
REDOX SUBSTITUTIONS (all VI-fold)			
$^{VI}Ce^{4+} + {}^{VI}Fe^{2+} = {}^{VI}Ce^{3+} + {}^{VI}Fe^{3+}$			Favorable based on model, but Fe^{2+} likely rare in VII-fold site
$Ce^{4+} - Ce^{3+}$	-0.14		
$Fe^{3+} - Fe^{2+}$	-0.13	-0.01	
$Ce^{3+} - Fe^{2+}$	0.23		
$Ce^{4+} - Fe^{3+}$	0.22	0.01	
$^{VI}Ce^{4+} + {}^{VI}Mn^{3+} = {}^{VI}Ce^{3+} + {}^{VI}Mn^{4+}$			Favorable based on model, but Mn^{4+} is uncommon in silicates and its presence needs to be evaluated
$Ce^{4+} - Ce^{3+}$	-0.14		
$Mn^{4+} - Mn^{3+}$	-0.12	-0.02	
$Ce^{3+} - Mn^{3+}$	vertical		
$Ce^{4+} - Mn^{4+}$	vertical	0	
$^{VI}Ce^{4+} + {}^{VI}Mn^{2+} = {}^{VI}Ce^{3+} + {}^{VI}Mn^{3+}$			Favorable based on model, but Mn^{2+} likely rare in VII-fold site
$Ce^{4+} - Ce^{3+}$	-0.14		
$Mn^{3+} - Mn^{2+}$	-0.18	0.04	
$Ce^{3+} - Mn^{2+}$	0.18		
$Ce^{4+} - Mn^{3+}$	0.22	-0.04	
$^{VI}Ce^{4+} + {}^{VI}Cr^{3+} = {}^{VI}Ce^{3+} + {}^{VI}Cr^{4+}$			Less favorable
$Ce^{4+} - Ce^{3+}$	-0.14		
$Cr^{4+} - Cr^{3+}$	-0.07	-0.07	
$Ce^{3+} - Cr^{3+}$	∞		
$Ce^{4+} - Cr^{4+}$	∞	0	
$^{VI}Ce^{4+} + {}^{VI}V^{3+} = {}^{VI}Ce^{3+} + {}^{VI}V^{4+}$			Less favorable
$Ce^{4+} - Ce^{3+}$	-0.14		
$V^{4+} - V^{3+}$	-0.06	-0.08	
$Ce^{3+} - V^{3+}$	∞		
$Ce^{4+} - V^{4+}$	∞	0	
$^{VI}Ce^{4+} + {}^{VI}V^{4+} = {}^{VI}Ce^{3+} + {}^{VI}V^{5+}$			Less favorable
$Ce^{4+} - Ce^{3+}$	-0.14		
$V^{5+} - V^{4+}$	-0.04	-0.10	
$V^{4+} - Ce^{3+}$	-0.43		
$V^{5+} - Ce^{4+}$	-0.33	-0.10	
$^{VI}Ce^{4+} + {}^{VI}(Nb,Ta)^{4+} = {}^{VI}Ce^{3+} + {}^{VI}(Nb,Ta)^{5+}$			Less favorable
$Ce^{4+} - Ce^{3+}$	-0.14		
$(Nb,Ta)^{5+} - (Nb,Ta)^{4+}$	-0.04	-0.10	
$(Nb,Ta)^{4+} - Ce^{3+}$	-0.33		
$(Nb,Ta)^{5+} - Ce^{4+}$	-0.23	-0.10	

673 **Table 5:** Continued.
674

Substitution / couple	**Slope** $(r_i-r_o)/(\Delta valence)$	**Line pair slope difference**	**Comments**
$^{VII}Ce^{3+}$ SUBSTITUTIONS			
$^{VII}Ce^{3+} + {}^{VI}Ti^{4+} = {}^{VII}Ca^{2+} + {}^{VI}(Nb,Ta)^{5+}$			Favorable based on model
$Ce^{3+} – Ca^{2+}$	0.01		
$(Nb,Ta)^{5+} – Ti^{4+}$	0.04	-0.03	
$Ti^{4+} – Ca^{2+}$	-0.46		
$(Nb,Ta)^{5+} – Ce^{3+}$	-0.43	-0.03	
$^{VII}Ce^{3+} + {}^{VI}Al^{3+} = {}^{VII}Ca^{2+} + {}^{VI}Ti^{4+}$			Favorable based on model
$Ce^{3+} – Ca^{2+}$	0.01		
$Ti^{4+} – Al^{3+}$	0.06	-0.05	
$Al^{3+} – Ca^{2+}$	-0.52		
$Ti^{4+} – Ce^{3+}$	-0.47	-0.05	
$^{VII}Ce^{3+} + {}^{VI}V^{3+} = {}^{VII}Ca^{2+} + {}^{VI}Ti^{4+}$			Favorable based on model
$Ce^{3+} – Ca^{2+}$	0.01		
$Ti^{4+} – V^{3+}$	-0.04	0.05	
$V^{3+} – Ca^{2+}$	-0.42		
$Ti^{4+} – Ce^{3+}$	-0.47	0.05	
$^{VII}Ce^{3+} + {}^{VI}Fe^{3+},Mn^{3+} = {}^{VII}Ca^{2+} + {}^{VI}Ti^{4+}$			Favorable based on model
$Ce^{3+} – Ca^{2+}$	0.01		
$Ti^{4+} – Fe^{3+}$	-0.05	0.06	
$Fe^{3+} – Ca^{2+}$	-0.41		
$Ti^{4+} – Ce^{3+}$	-0.47	0.06	
$^{VI}Ce^{3+}/{}^{VI}Ce^{4+}$ COUPLED SUBSTITUTIONS			
$^{VI}Ce^{4+} + {}^{VI}(Nb,Ta)^{4+} = {}^{VI}Ce^{3+} + {}^{VI}V^{5+}$			Favorable based on model, but unlikely if $(Nb,Ta)^{4+}$ and/or V^{5+} contents are low
$Ce^{4+} – Ce^{3+}$	-0.14		
$V^{5+} – (Nb,Ta)^{4+}$	-0.14	0	
$(Nb,Ta)^{4+} – Ce^{3+}$	-0.33		
$V^{5+} – Ce^{4+}$	-0.33	0	
$^{VI}Ce^{4+} + {}^{VI}Zr^{4+} = {}^{VI}Eu^{3+} + {}^{VI}(Nb,Ta)^{5+}$			Favorable based on model, but unlikely because Eu^{3+} content may be low
$Ce^{4+} – Eu^{3+}$	-0.08		
$(Nb,Ta)^{5+} – Zr^{4+}$	-0.08	0	
$Zr^{4+} – Eu^{3+}$	-0.23		
$(Nb,Ta)^{5+} – Ce^{4+}$	-0.23	0	

675

SUPPLEMENTARY MATERIAL

Resonant Inelastic X-ray Scattering (RIXS) confirmation of Ce^{3+}/Ce^{4+}

Because the Ce L_3 – edge XANES is dominated by the Ce^{3+} white line, one cannot be absolutely certain that the intensity variation in the higher energy XANES peak originates from Ce^{4+}; therefore, we also used RIXS to confirm, at least qualitatively, the presence of Ce^{4+}. In the RIXS technique, as the excitation energy approaches the Ce L_3 – edge (Fig. S1a, c, e), the inelastically scattered X-ray exhibits distinctly different features between Ce^{3+} and Ce^{4+} due to the presence and the absence of a 4*f* electron respectively. The analysis of the RIXS process is discussed elsewhere (e.g., Sham et al., 2005; Rubensson, 2000).

To examine the RIXS behavior for Ce^{3+} and Ce^{4+}, we analyzed the model compounds ($CePO_4$ and CeO_2) at a range of different excitation energies in the pre-edge region of the XANES spectra. The RIXS spectra for these compounds are presented using X-ray emission intensity versus emission wavelength (Fig. S1). The $CePO_4$ compound displays a normal RIXS behavior (Fig. S1b) showing a gradual increase in intensity and an energy dispersion of the $L\alpha_{1,2}$ (shift to lower emission wavelength) as the excitation energy approaches the threshold (Bartolome et al., 1999). However, the CeO_2 compound (Fig. S1d) exhibits a more complex pattern as the excitation energy approaches the threshold (number 13 in Fig. S1c). Instead of a well-defined $L\alpha_{1,2}$ –like doublet, the RIXS spectra appear to be a considerably broadened multiplet (Fig. S1d) while a gradual increase in intensity and a characteristic energy dispersion can still be observed. This anomaly in Ce^{4+} RIXS has been attributed to $f^1 (2p)^6$ to $f^2 (2p)^5$ quadrupole transition (Hague et al. 2004, Sham et al. 2005).

The XANES spectra for the green titanite at the Ce L_3 – edge and the pre-edge region is shown in Figure S1e. In the pre-edge region, where the RIXS is most sensitive to the oxidation

state, the green titanite RIXS (Fig. S1f) resembles neither the clean doublet of the Ce^{3+} (Fig. S1b) nor the broadened multiplet of the Ce^{4+} (Fig. S1d), but a mixture. Although the green titanite spectra are noisy due to the low concentration of Ce, it is possible to qualitatively examine the spectra. For example, at ~5720 eV excitation energy the green titanite RIXS shows a doublet (Fig. S1f) reminiscent of Ce^{3+} but the main peak is significantly distorted and at lower excitation energy, the shoulder (emerging to become $L\alpha_2$) that was clearly noticeable in the Ce^{3+} RIXS was not detected. These observations are consistent with a mixed contribution from both oxidation states.

SUPPLEMENTARY REFERENCES

Bartolome, F., Kirsch, M.H., Raoux, D., and Tonnerre, J.-M. (1999) Quadrupole excitation channels at the L_3-edge of rare-earth ions probed by Resonant Inelastic Scattering. Physical Review, B60, 13497-13506.

Hague, C.F., Mariot, J.-M., Delaunay, R., Gallet, J.-J., Journel, L., Rueff, J.-P. (2004) Resonant X-ray emission spectroscopy applied to a mixed-valent system. Journal of Electron Spectroscopy and Related Phenomena, 136, 179-183.

Rubensson, J.-E. (2000) RIXS dynamics for beginners. Journal of Electron Spectroscopy and Related Phenomena, 110-111, 135-151.

Sham, T.K., Gordon, R.A., and Heald, S.M. (2005) Resonant inelastic scattering at the Ce L_3 edge of $CePO_4$ and CeO_2: implications for the valence of CeO_2 and related phenomena. Physical Review, B72, 035113 (1-6).

FIGURE S1: a) XANES spectra showing excitation energies used for the RIXS investigations of $Ce^{3+}PO_4$. b) RIXS spectra for the $Ce^{3+}PO_4$ compound. c) XANES spectra showing excitation energies used for the RIXS investigations of $Ce^{4+}O_2$. d) RIXS spectra for the $Ce^{4+}O_2$ compound. e) XANES spectra showing excitation energies used for the RIXS investigations of the green titanite. f) RIXS spectra for the green titanite.

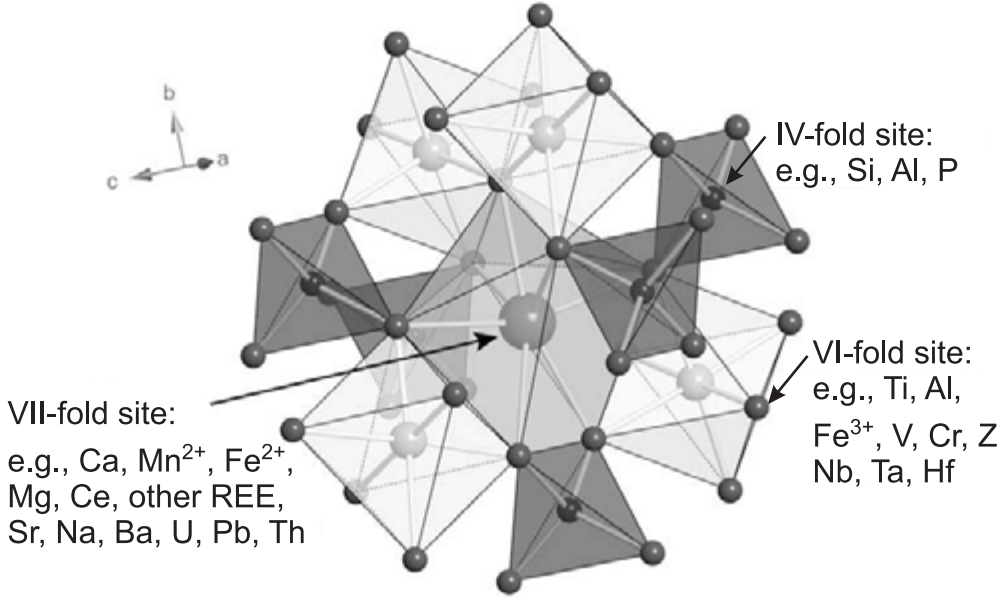

Titanite - Figure 1

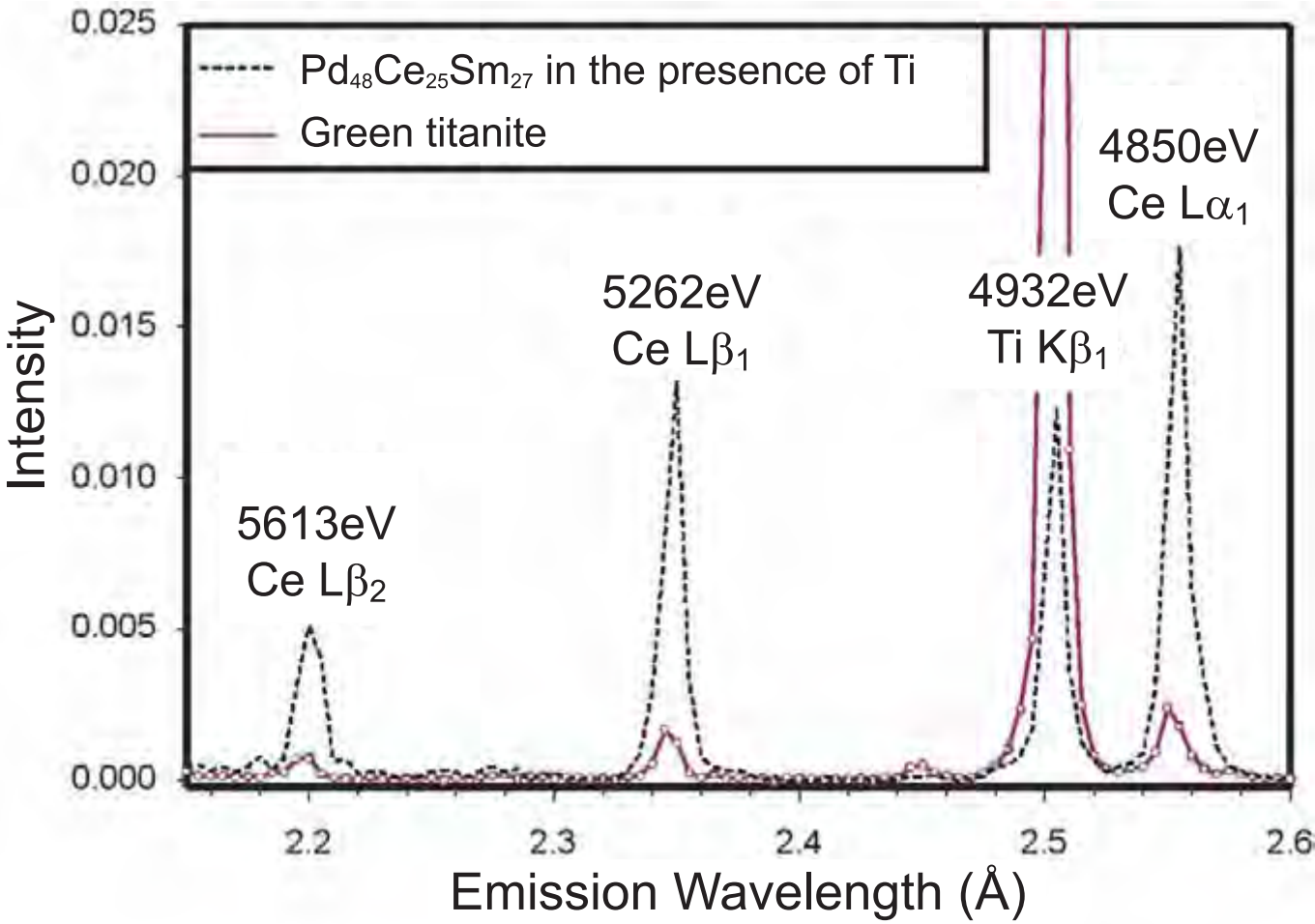

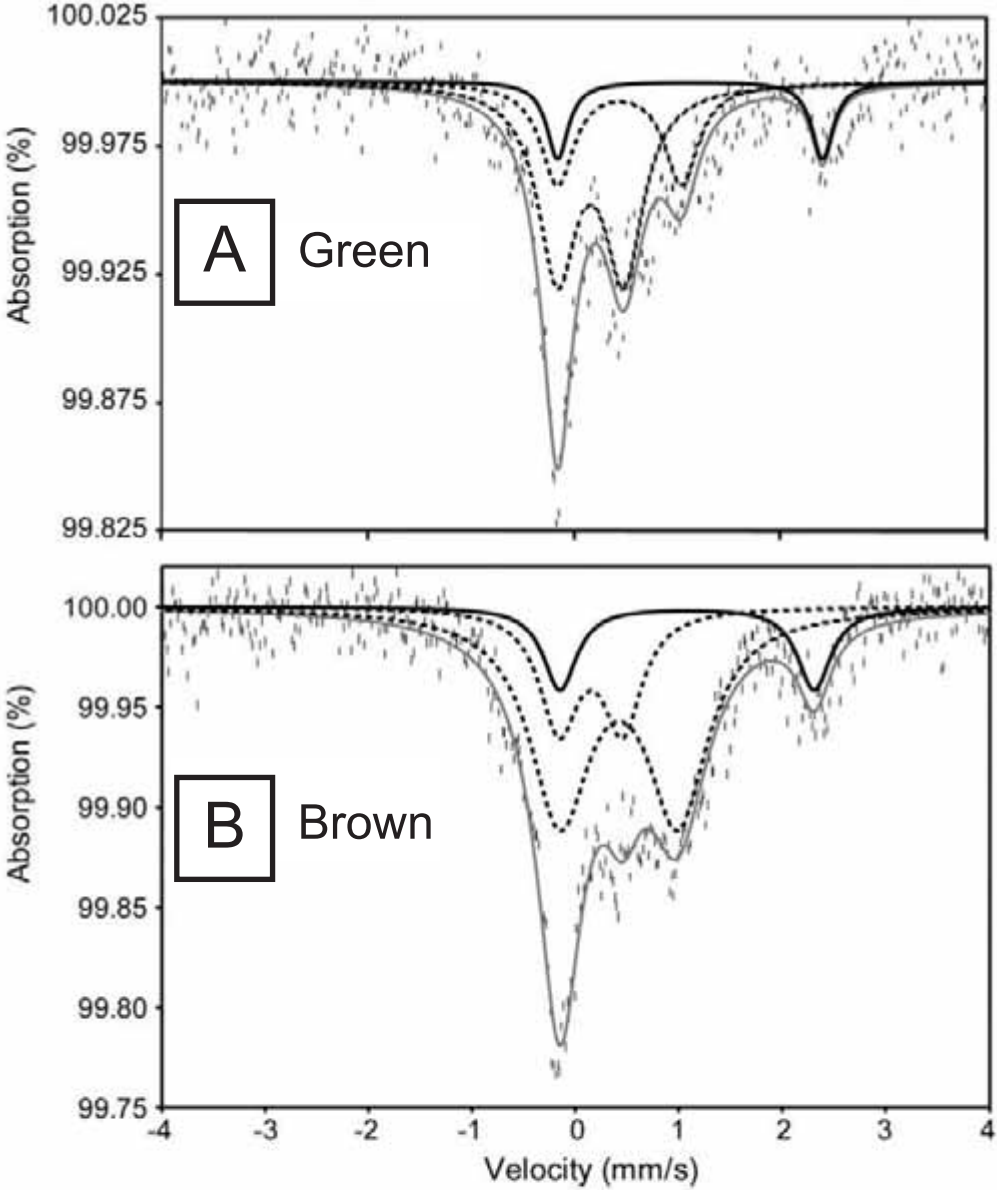

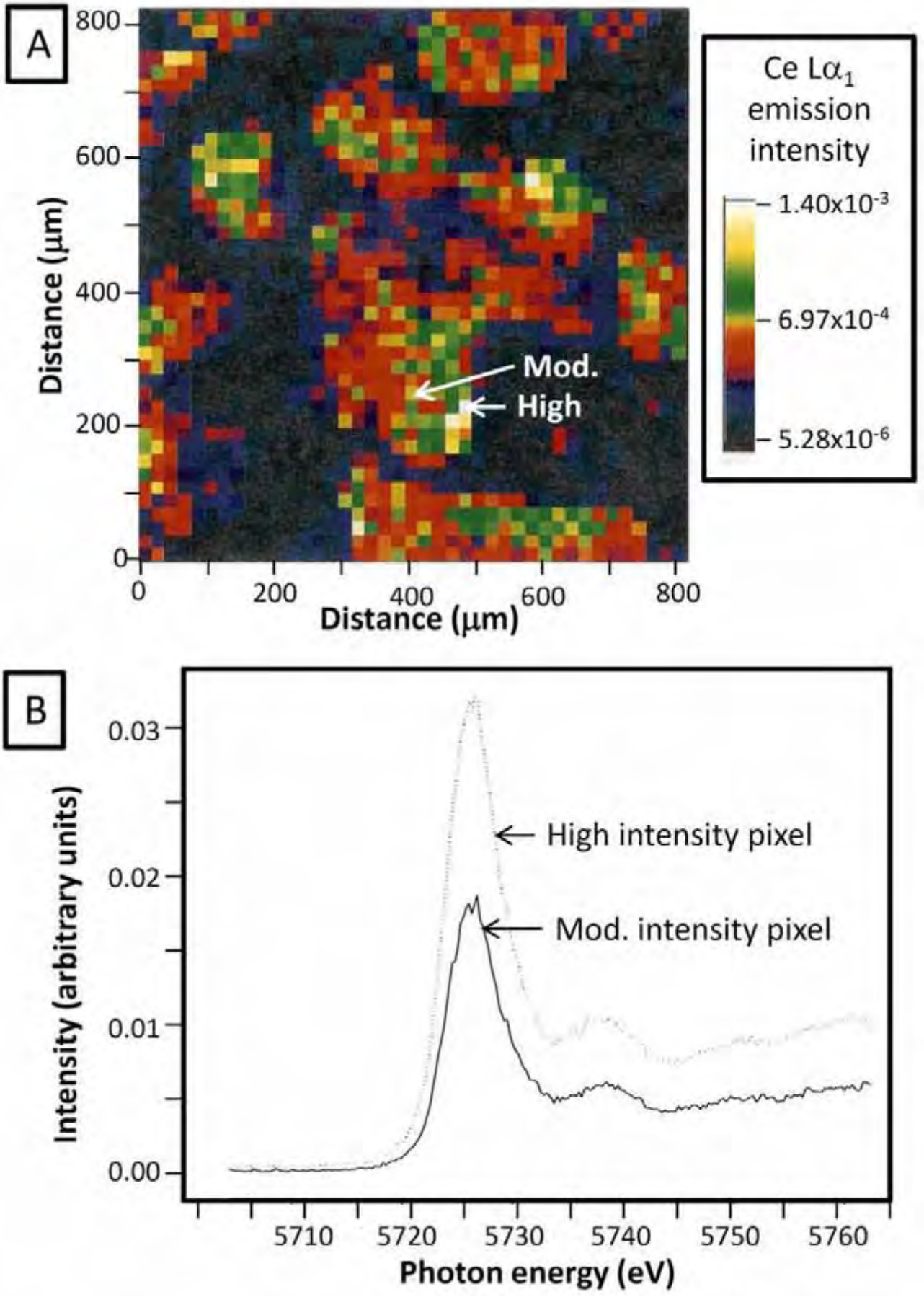

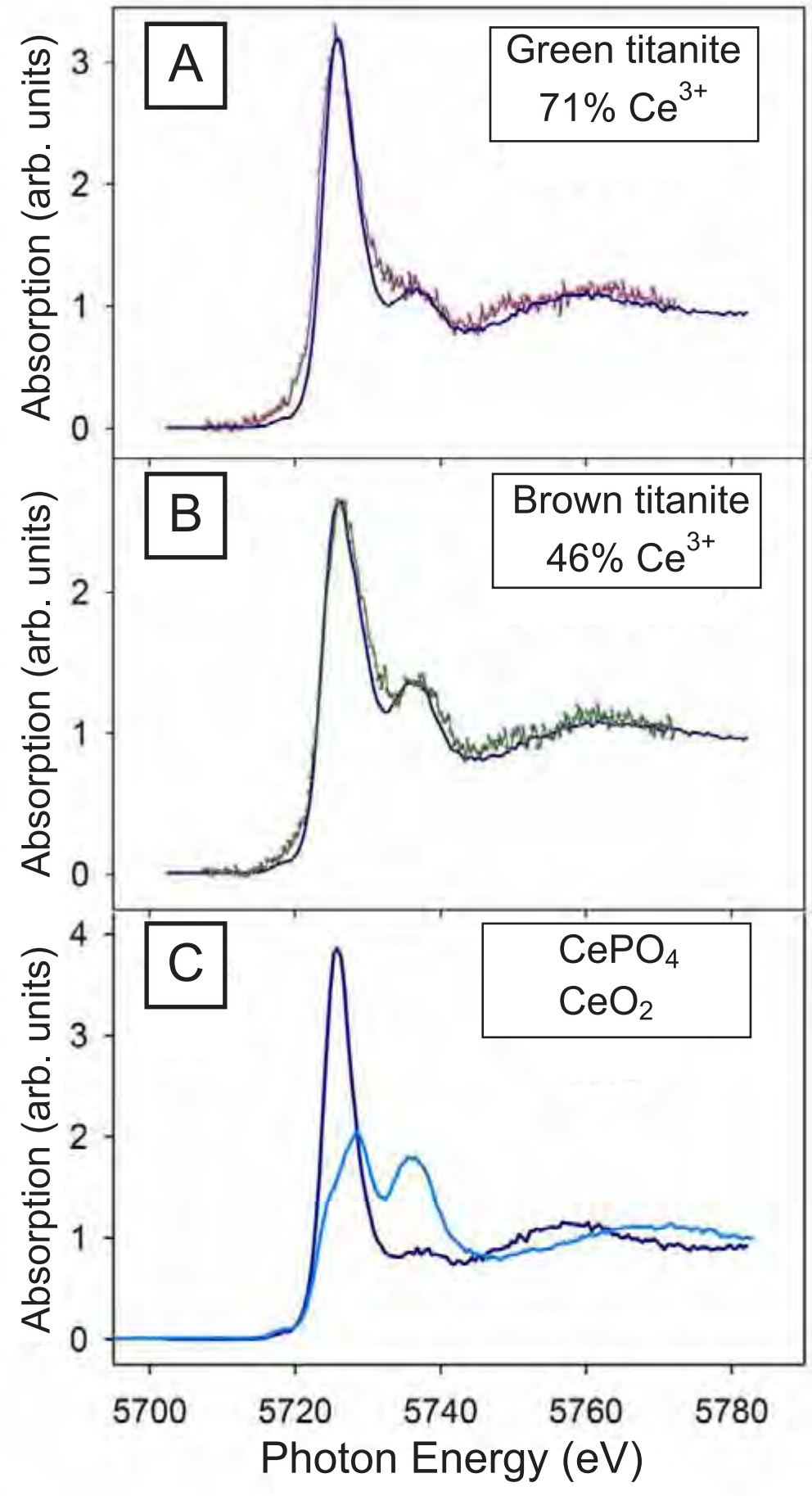

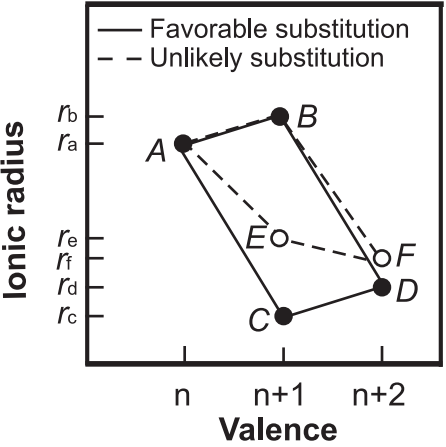

Titanite - Figure 6

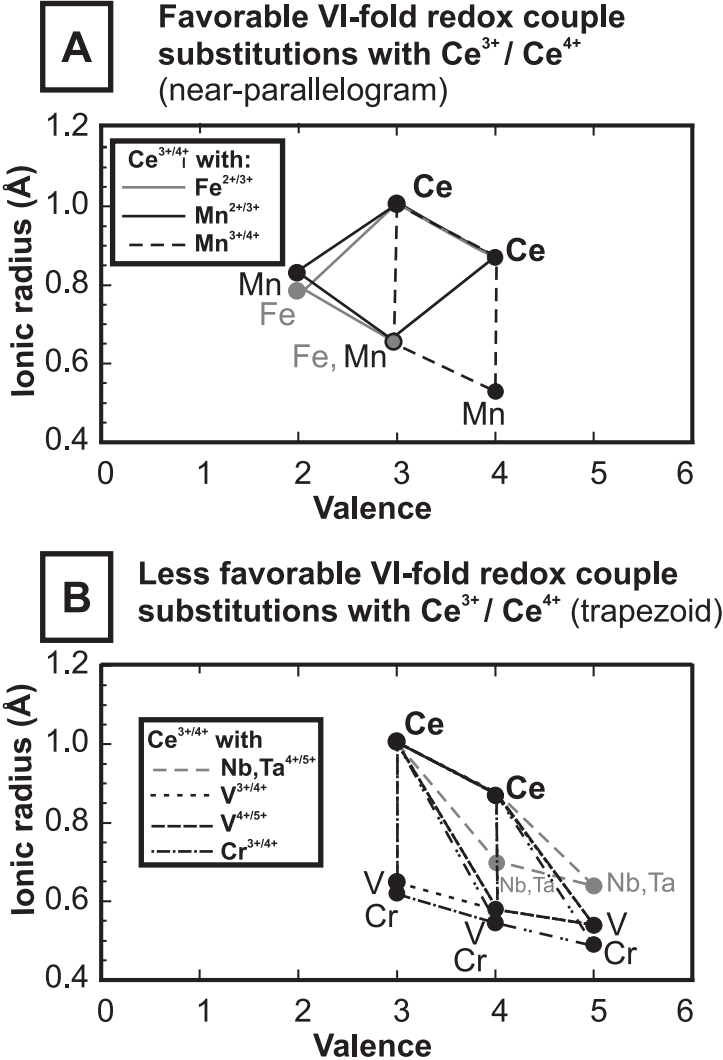

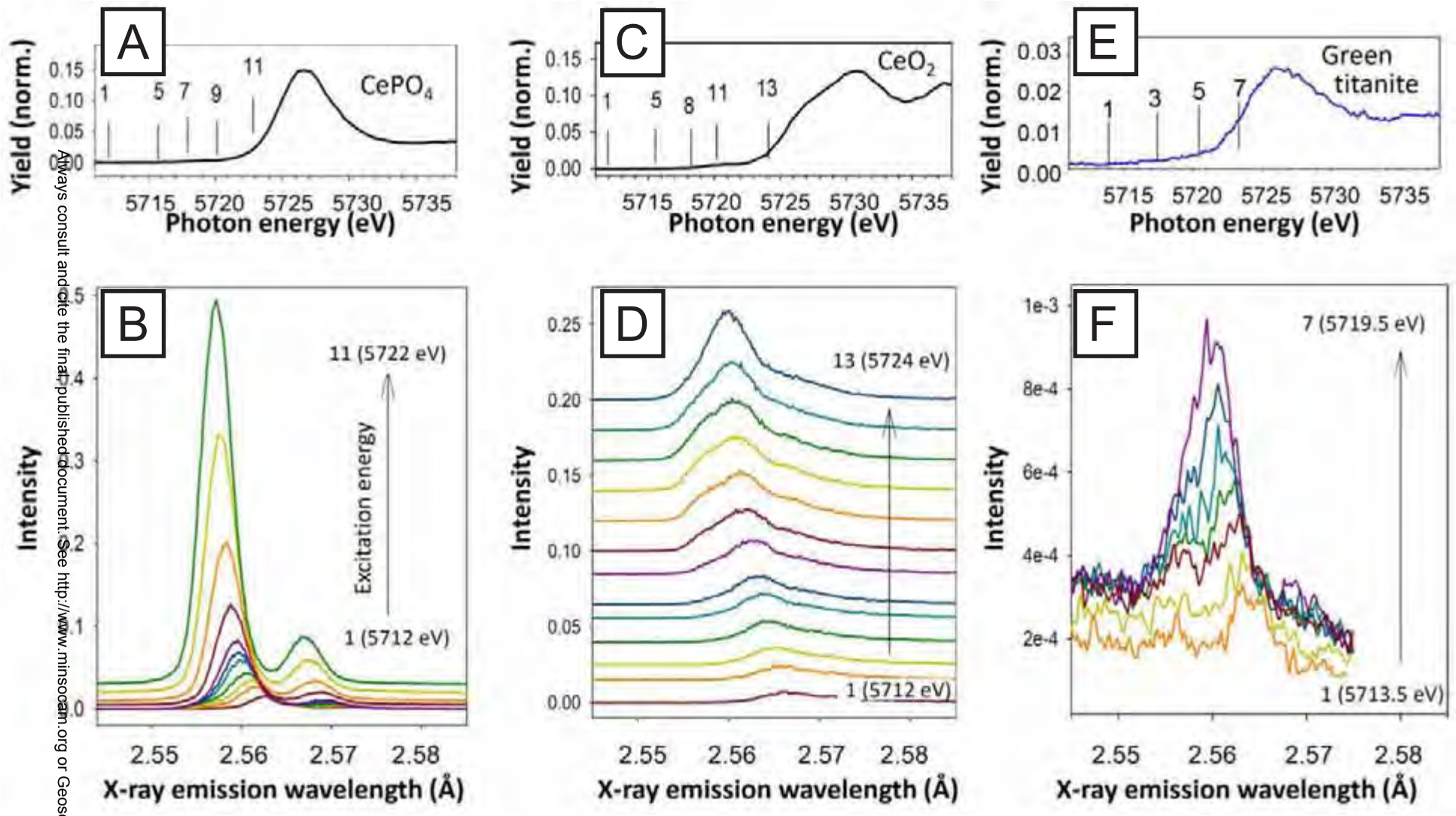

Titanite - Supplement Figure S1